J. Fluid Mech. (2011), *vol.* 680, *pp.* 417–434. © Cambridge University Press 2011
doi:10.1017/jfm.2011.169

Freely decaying, homogeneous turbulence generated by multi-scale grids

P.-Å. KROGSTAD[1]† AND P. A. DAVIDSON[2]

[1]Department of Energy and Process Engineering, Norwegian University of Science and Technology, N-7491 Trondheim, Norway

[2]Department of Engineering, University of Cambridge, Cambridge CB2 1PZ, UK

(Received 13 May 2010; revised 26 January 2011; accepted 4 April 2011; first published online 19 May 2011)

We investigate wind-tunnel turbulence generated by both conventional and multi-scale grids. Measurements were made in a tunnel which has a large test section, so that possible side wall effects are very small and the length ensures that the turbulence has time to settle down to a homogeneous shear-free state. The conventional and multi-scale grids were all designed to produce turbulence with the same integral scale, so that a direct comparison could be made between the different flows. Our primary finding is that the behaviour of the turbulence behind our multi-scale grids is virtually identical to that behind the equivalent conventional grid. In particular, all flows exhibit a power-law decay of energy, $u^2 \sim t^{-n}$, where n is very close to the classical Saffman exponent of $n = 6/5$. Moreover, all spectra exhibit classical Kolmogorov scaling, with the spectra collapsing on the integral scales at small k, and on the Kolmogorov microscales at large k. Our results are at odds with some other experiments performed on similar multi-scale grids, where significantly higher energy decay exponents and turbulence levels have been reported.

Key words: homogeneous turbulence, turbulence theory, turbulent mixing

1. Introduction

In recent years a number of wind-tunnel experiments and numerical simulations have focused on quasi-homogeneous turbulence generated by multi-scale grids (see, for example, Hurst & Vassilicos 2007; Nagata *et al.* 2008). When the grids concerned possess certain fractal-like properties, this is sometimes referred to as fractal-generated turbulence. In some of these experiments, the turbulence appears to behave in unexpected ways. For example, Hurst & Vassilicos (2007) report unusually high values of $Re_\lambda = u\lambda/\nu$, perhaps twice that associated with the equivalent conventional grid (here λ is the Taylor microscale, $\lambda^2 = \langle u_x^2 \rangle / \langle (\partial u_x/\partial x)^2 \rangle$, ν is the viscosity, and $u = \sqrt{\langle \boldsymbol{u}^2 \rangle / 3}$ is the characteristic fluctuating velocity). They also report energy decay characteristics, such as power-law decay, $\langle \boldsymbol{u}^2 \rangle \sim t^{-n}$, with very high decay exponents ($n \sim 2$ rather than the classical $n \sim 1.2$–1.4), and also exponential decay rate for some grid geometries. This is surprising as there are good arguments why classical fully developed homogeneous turbulence can decay no faster than $n \sim 10/7$ (see e.g. the Appendix of this paper; Krogstad & Davidson 2010 and Ossai & Lesieur 2000 for a summary of these arguments). The implication is that turbulence generated by

† Email address for correspondence: per.a.krogstad@ntnu.no

https://doi.org/10.1017/jfm.2011.169 Published online by Cambridge University Press

multi-scale excitation can exhibit non-classical characteristics, which has led to a re-examination of the assumptions underlying energy decay laws (see for example George & Wang 2009; Hosokawa 2008).

However, this suggestion is somewhat at odds with the evidence of direct numerical simulations in periodic cubes, where it is usually found that, after some transient, the behaviour of the turbulence is largely independent of the precise form of the initial energy spectrum (see, for example, Ossai & Lesieur 2000). Indeed, it is often argued that, once fully developed, all the turbulence remembers of its initial conditions is the prefactor, c_m, in the expression $E(k \to 0) = c_m k^m$, c_m being an invariant for $m \leqslant 4$ (Ossai & Lesieur 2000; Davidson 2004, 2009; Ishida, Davidson & Kaneda 2006).

There is, however, a different interpretation of the experiments of Hurst & Vassilicos (2007), which is consistent with the evidence of the numerical simulations. Immediately behind a multi-scale grid the turbulence is far from homogeneous, and there is a significant production of turbulent energy due to transverse gradients in the mean velocity. Moreover, this inhomogeneity in the mean and fluctuating velocities is stronger than for a conventional grid and it persists for many tens of integral scales downstream of the mesh (Nagata *et al.* 2008). This might not matter if all measurements are made well downstream of a multi-scale grid, where approximate homogeneity is recovered. In conventional grid turbulence it is considered good practice to restrict measurements to, say, $x > 25$–$30\,M$ in order to avoid the inhomogeneous region behind the grid (e.g. Comte-Bellot & Corrsin 1966; Gad-el-Hak & Corrsin 1974). It is possible, therefore, that the apparently non-classical results obtained for some of the grid geometries of Hurst & Vassilicos (2007) are a consequence of a distinct lack of homogeneity immediately behind the grid, i.e. a transient phenomenon which disappears further downstream. Indeed, Hurst & Vassilicos (2007) note that more extensive tests are required in order to assess the role of inhomogeneities close to the grid.

In order to test the hypothesis that turbulence behind multi-scale grids will develop in a classical way (after an initial transient), we have conducted a series of wind-tunnel experiments using two multi-scale grids of the cross-class described in Hurst & Vassilicos (2007), and compared these results with data obtained using a conventional grid. In order to ensure that the comparison is meaningful, the dimensions of the grids were chosen such that the integral scale of the turbulence some short distance downstream of each grid, ℓ_0, is virtually the same in all three cases (within a per cent or so). Crucially, the experiments were carried out in a large working section, and measurements taken over the extended range $80\ell_0 < x < 400\ell_0$, which translates to $50\,M < x < 240\,M$ for the conventional grid. Excellent homogeneity was obtained throughout the measurement range for all three grids and the long working section allowed us to determine the energy decay characteristics with considerable accuracy. As we shall see, the fully developed turbulence generated by all three grids is virtually identical. In particular, there is no significant difference in the behaviour of Re_λ, and in all cases the decay exponent n in the expression $\langle \boldsymbol{u}^2 \rangle \sim t^{-n}$ is very close to the classical prediction of Saffman (1967), i.e. $n = 6/5$. (For a discussion of decay exponents in classical turbulence, see e.g. Davidson 2004 and Krogstad & Davidson 2010.)

2. The experimental set-up

The experiments were performed in the large recirculating wind tunnel described in Krogstad & Davidson (2010). The tunnel test section has transverse dimensions

https://doi.org/10.1017/jfm.2011.169 Published online by Cambridge University Press

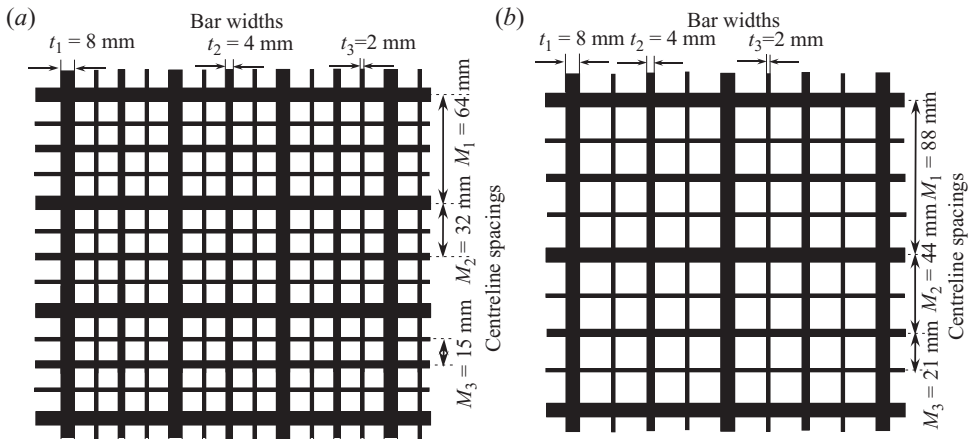


FIGURE 1. (a, b) The two multi-scale grids used in this study.

of 2.7 m × 1.8 m (measured at the start of the test section) and is 12 m long. There is an adjustable roof to compensate for the growth of the sidewall boundary layers and the grids were mounted upstream in the test section contraction to improve isotropy. From the location of the grid to the entrance of the test section, the area contraction ratio was 1.48 and the test section starts $x = 1.2$ m downstream of the grid.

All three grids were produced from a 2 mm thick metal sheet. The conventional grid (labelled *cg*) has square holes 30 mm × 30 mm punched at 40 mm spacing, giving a mesh size of $M = 40$ mm, a bar width of $t = 10$ mm, and a solidity of $\sigma = 44\,\%$. The tests on this grid were all performed at a Reynolds number of $Re_M = UM/\nu = 3.6 \times 10^4$, where $U = 13.5\,\mathrm{m\,s^{-1}}$ was the mean speed in the tunnel.

The first of the multi-scale grids labelled *msg*1 is similar to the cross-grid type (a) of Hurst & Vassilicos (2007) (which we shall label $cg-a$) and is shown in figure 1(*a*). It has bar widths ranging from $t_1 = 8$ mm down to $t_3 = 2$ mm, and mesh sizes ranging from $M_1 = 64$ mm to $M_3 = 15$ mm. The solidity of *msg*1 is also $\sigma = 44\,\%$. These measurements were taken at $U = 14.0\,\mathrm{m\,s^{-1}}$.

The second multi-scale grid (*msg*2) is shown in figure 1(*b*). As for *msg*1, the bar widths vary from $t_1 = 8$ mm down to $t_3 = 2$ mm, though the mesh sizes are larger, with $M_1 = 88$ mm to $M_3 = 21$ mm. This reduces the solidity of *msg*2 to $\sigma = 33\,\%$. This grid was tested at $U = 15.5\,\mathrm{m\,s^{-1}}$.

As we shall see, the turbulence produced by these grids becomes more or less homogeneous and fully developed at around $x = 2$ m, where the Kolmogorov microscale is $\eta \approx 0.22$–0.26 mm. On the other hand, the integral scales at $x = 2$ m, $\ell_0 = \ell(x = 2\,\mathrm{m})$, obtained in the usual way by integrating the longitudinal correlation function

$$\ell = \int_0^\infty \frac{\langle u_x(x)u_x(x+r)\rangle}{\langle u_x^2\rangle}\,\mathrm{d}r, \tag{2.1}$$

turn out to be $\ell_0 = 23.9$ mm (for *cg*), $\ell_0 = 23.6$ mm (for *msg*1), and $\ell_0 = 23.4$ mm (for *msg*2), respectively. (The measurements of η and ℓ are discussed in § 5.) Note the uniformity of ℓ_0 across the grids. Note also that the geometric length scales associated with the two multi-scale grids almost span the range of dynamic scales associated with the turbulence, from around 9η up to several integral scales. Finally, we note that, in terms of ℓ_0, the tunnel cross-section is approximately $115\ell_0 \times 80\ell_0$, thus ensuring that there is minimal influence of the side-wall boundary layers. Measurements are taken

https://doi.org/10.1017/jfm.2011.169 Published online by Cambridge University Press

up to a considerable distance downstream of the grid, allowing an accurate estimate of the energy decay exponent, n.

The data were obtained using single- and two-component hot-wire anemometry. For the measurements of the decay of $\langle (u_x)^2 \rangle$, spectra, the length scales η and ℓ etc. a purpose made 2.5 μm partly etched platinum-10 % rhodium straight single-wire probe was produced. The active wire length was 0.5 mm. For two-component measurements and for global checks such as spanwise homogeneity, an X-wire probe with $\pm 45^\circ$ nominal wire angles was produced. For this probe, 5 μm partly etched wires were used with 1 mm wire lengths. The two wires were also separated in the spanwise direction by $\Delta z = 1$ mm. By careful handling of the two delicate probes, it was possible to maintain the same wires throughout the whole experiment. Hence there should be no effects in the data that can be attributed to changes in probe characteristics.

The probes were operated at an overheat temperature of about 320° using in-house manufactured anemometers which were tuned to a frequency response f_w of at least 20 kHz (f_w is here calculated from $f_w = (1.3\tau)^{-1}$, where τ is the time for the anemometer output to recover within 10 % of the asymptotic level after a square wave step change has been inserted on the top of the Whetstone bridge in the anemometer). The output from the anemometers was suitably offset and amplified to span as much as possible of the ± 10 volt range of the 16 bit acquisition card used before the signals were passed through an AC coupled Krohn-Hite amplifier and low-pass filter unit. The filter frequency f_c was set by inspecting the dissipation spectra of a few initial measurements with very high filter settings. Then, f_c was set at a frequency where noise first started to affect the dissipation spectra and a new set of data was obtained at a sampling frequency which was slightly higher than $2f_c$.

For verification purpose only, a number of two-component laser Doppler anemometry (LDA) measurements were taken for each grid, but these data were not used in the data analysis presented here, since LDA tends to produce too high turbulence levels as the turbulence intensity drops below about 1 %. Further information about the instrumentation and data analysis may be found in Krogstad & Davidson (2010).

3. Tests for homogeneity and isotropy

We start by documenting the relative degree of homogeneity and isotropy in the experiment. Figure 2 shows the time-averaged centreline velocity, normalized by $U_0 = U(x = 2\,\mathrm{m})$, for all three grids as a function of x. For $x > 2$ m, U is constant to within ± 0.5 %, with $Re = U\ell_0/\nu = 2.1 \times 10^4$, 2.2×10^4 and 2.4×10^4, respectively, for the three grids. However, for $x < 2$ m there is a noticeable streamwise acceleration due to the effect of the contraction extending slightly into the first part of the test section. In the light of the streamwise acceleration, we shall ignore data for $x < 2$ m (i.e. $x < 80\ell_0$). Figure 2 also shows the streamwise variation of $Re_\lambda = \langle u_x^2 \rangle^{1/2} \lambda/\nu$ for all three grids. The present values are only about one third of those reported by Hurst & Vassilicos (2007) and there is no significant difference between the conventional and multi-scale grids.

The spanwise distributions of the turbulence intensity, $T_u = u/U$, where $u = \langle u_x^2 \rangle^{1/2}$, measured at $x \approx 2$ m and $x \approx 6$ m are shown in figure 3, along with the spanwise distribution of the skewness, S_u, and flatness, F_u, of u_x at $x \approx 2$ m. The measurements were made over a span corresponding to about $z \approx \pm 4\,M$, where M represents the

https://doi.org/10.1017/jfm.2011.169 Published online by Cambridge University Press

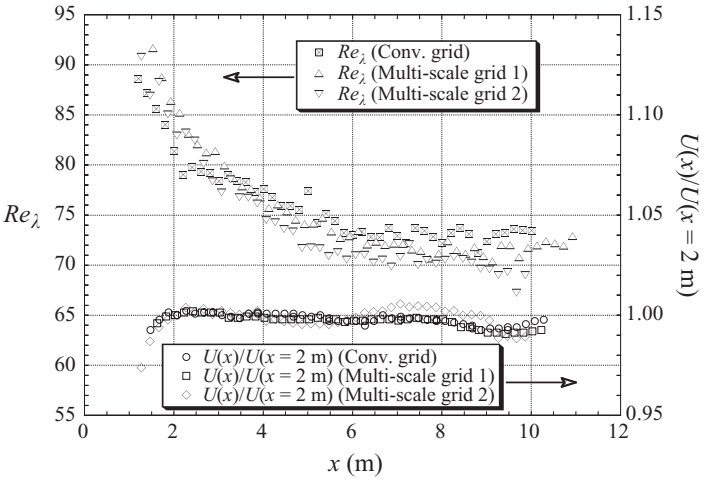


FIGURE 2. Streamwise distributions of Re_λ (left axis) and the test section centreline speed, U, (right axis). U is normalized by U at $x = 2\,\mathrm{m}$.

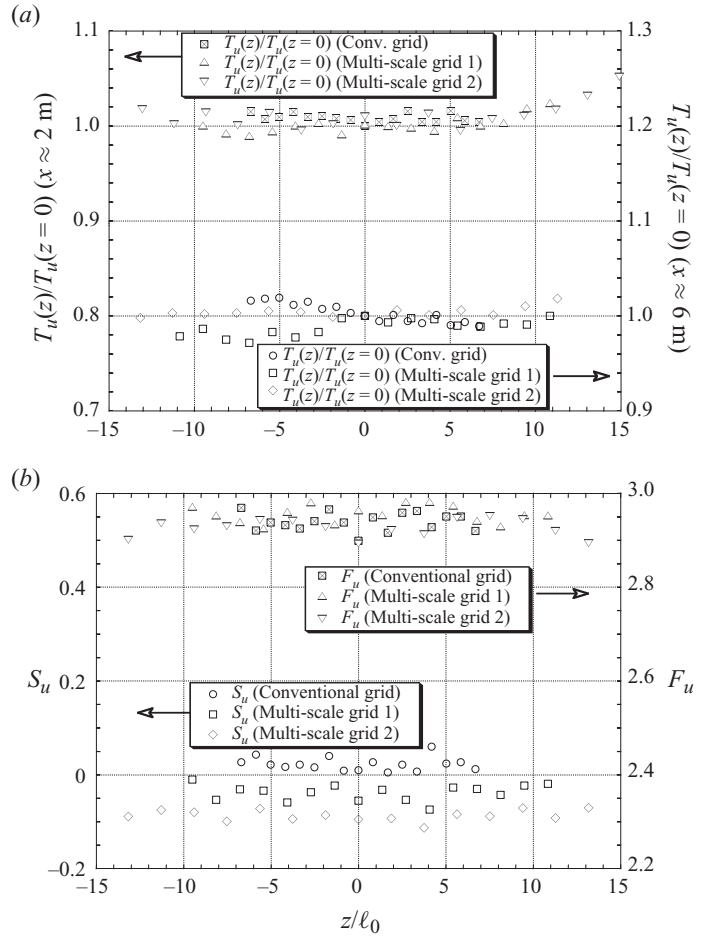


FIGURE 3. Spanwise distributions of (*a*) T_u at $x \approx 2\,\mathrm{m}$ (left axis) and $x \approx 6\,\mathrm{m}$ (right axis), and (*b*) skewness, S_u, of u_x (left axis) and flatness, F_u, of u_x at $x = 2\,\mathrm{m}$ (right axis).

https://doi.org/10.1017/jfm.2011.169 Published online by Cambridge University Press

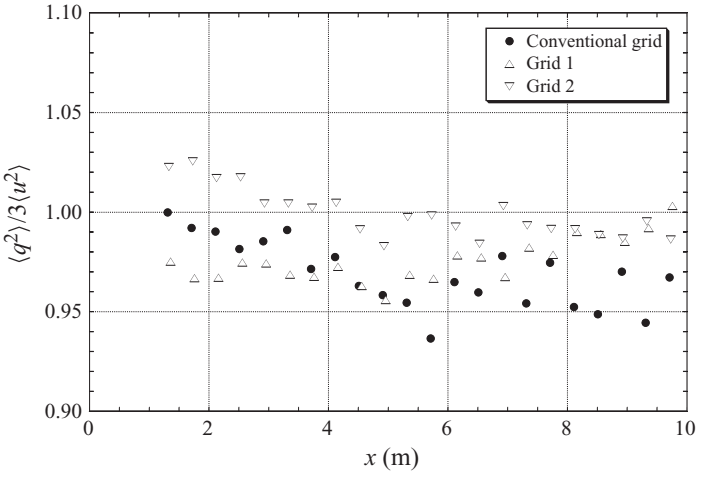


FIGURE 4. Streamwise distributions of $\langle q^2\rangle/3\langle u_x^2\rangle$.

largest mesh of each grid. Since M is only a well-defined scaling length for the conventional grid, we have chosen to scale z with ℓ_0, hence the apparent differences in the measurement range in the figure.

Again, all three grids are seen to behave in a similar manner, with variations in T_u limited to about $\pm 3\,\%$ at $x = 2\,\mathrm{m}$ and $\pm 2\,\%$ at $x = 6\,\mathrm{m}$. The skewness and flatness distributions are also well behaved in all three cases, with S_u being slightly negative and $F_u \approx 2.95$, values which are typical of most grid turbulence experiments. We conclude that, for $x > 2\,\mathrm{m}$, the turbulence is relatively homogeneous.

The streamwise development of the anisotropy of the turbulence, as measured by the ratios $\langle u_x^2\rangle/\langle u_y^2\rangle$, $\langle u_x^2\rangle/\langle u_z^2\rangle$ and $\langle q^2\rangle/3\langle u_x^2\rangle$, where $\langle q^2\rangle = \langle \boldsymbol{u}^2\rangle = \langle u_x^2 + u_y^2 + u_z^2\rangle$, was measured for each grid (figure 4). For all cases, it was found to follow closely the distributions reported for the conventional grid in figure 3 of Krogstad & Davidson (2010). We show here just the three streamwise developments of $\langle q^2\rangle/3\langle u_x^2\rangle$ which is seen to be very similar for the three cases and the ratio is very close to the isotropic value of one. For all grids $\langle u_x^2\rangle/\langle u_y^2\rangle$, $\langle u_x^2\rangle/\langle u_z^2\rangle$ and $\langle q^2\rangle/3\langle u_x^2\rangle$ were close to unity at $x = 2\,\mathrm{m}$, but $\langle u_x^2\rangle/\langle u_y^2\rangle$ and $\langle u_x^2\rangle/\langle u_z^2\rangle$ were found to divert slowly with increasing x. The largest departure from isotropy was observed at the exit of the test section, where $\langle u_x^2\rangle/\langle u_z^2\rangle$ reached values in the range of 0.8–0.9. There was a corresponding growth in $\langle u_x^2\rangle/\langle u_y^2\rangle$, to produce the almost constant $\langle q^2\rangle/3\langle u_x^2\rangle$ ratios shown in the figure.

Figure 5 shows the skewness and flatness distributions of the streamwise fluctuations measured along the centreline of the test section. The flatness is constant throughout the measurement range at $F_u \approx 2.95$ for all grids. The skewness is slightly different for the grids initially, as shown in figure 3(b), but they all tend steadily towards $S_u \to 0$ as the flow develops downstream.

In most of what follows we shall restrict the analysis of our data to the region $x > 2\,\mathrm{m}$, to avoid any acceleration effects caused by the inhomogeneities in U, and to $x < 8\,\mathrm{m}$, because of the increased levels of noise for large x as the turbulence level drops well below 1 %. For completeness, however, the full set of data will be included in the plots so that the reader may see where and how the data depart from classical decay behaviour. From the data presented above we see that, in this range, the turbulence is reasonably homogeneous and that, although there is some

https://doi.org/10.1017/jfm.2011.169 Published online by Cambridge University Press

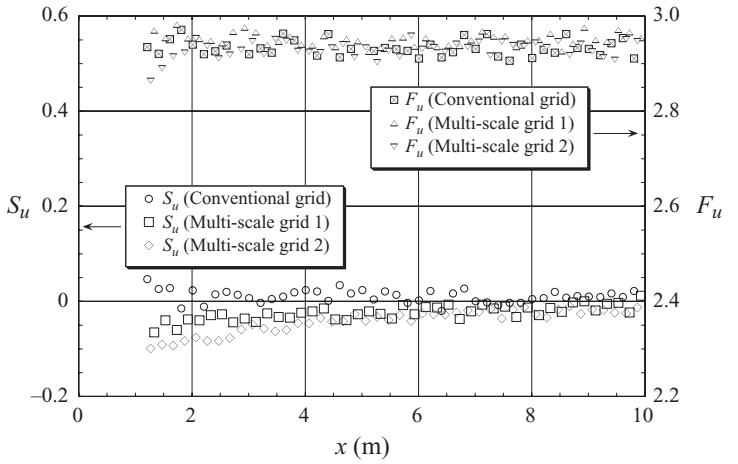


FIGURE 5. Streamwise distributions of skewness and flatness factors.

anisotropy, the levels are not excessive and are comparable to, if not better, than in most other experiments.

4. The energy decay rate

We shall now estimate the decay exponent, n, in the decay law $\langle \boldsymbol{u}^2 \rangle \sim t^{-n}$ for all three grids. First, however, perhaps it is worth saying something about the values this exponent might be expected to take on theoretical grounds. As noted by Davidson (2004, 2009) and Krogstad & Davidson (2010), there are two classical predictions for n. The first arises when $E(k \to 0) \sim k^2$, a situation called Saffman turbulence, and the other when $E(k \to 0) \sim k^4$, the so-called Batchelor turbulence. In the former case, it may be shown that

$$L = \int \langle \boldsymbol{u} \cdot \boldsymbol{u}' \rangle \, \mathrm{d}\boldsymbol{r} = \text{constant} \quad (\text{for } E(k) \sim k^2), \tag{4.1}$$

where $\langle \boldsymbol{u} \cdot \boldsymbol{u}' \rangle$ is the usual two-point velocity correlation (see Saffman 1967), while in the latter case

$$I = -\int r^2 \langle \boldsymbol{u} \cdot \boldsymbol{u}' \rangle \, \mathrm{d}\boldsymbol{r} = \text{constant} \quad (\text{for } E(k) \sim k^4), \tag{4.2}$$

with the caveat that (4.2) holds only once the turbulence is fully developed (see Ishida *et al.* 2006). These integrals are dominated by the large scales and so self-similarity of the large scales (when it applies) demands

$$u^2 \ell^3 = \text{constant} \quad (\text{for Saffman turbulence}), \tag{4.3}$$

$$u^2 \ell^5 = \text{constant} \quad (\text{for Batchelor turbulence}). \tag{4.4}$$

These may be combined with the empirical, but well-supported, law

$$\frac{\mathrm{d}u^2}{\mathrm{d}t} = -A \frac{u^3}{\ell}, \qquad A = \text{constant}, \tag{4.5}$$

to give $n = 6/5$ (Saffman exponent; see Saffman 1967) in the $E(k) \sim k^2$ turbulence, and $n = 10/7$ (Kolmogorov exponent; see Kolmogorov 1941) in the $E(k) \sim k^4$ turbulence. The first of these exponents was observed in the experiments of Krogstad & Davidson

https://doi.org/10.1017/jfm.2011.169 Published online by Cambridge University Press

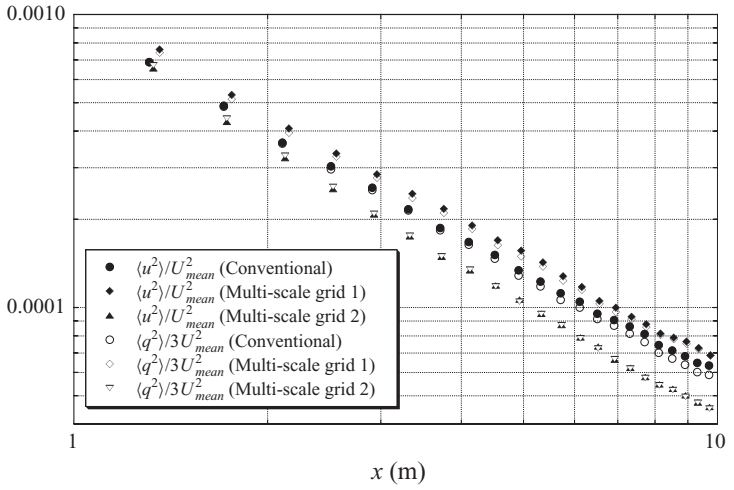


FIGURE 6. Streamwise distributions of $\langle u_x^2\rangle/U^2$ (filled symbols) and $\langle q^2\rangle/3U^2$ (open symbols).

(2010) and the second in the numerical simulations of Ishida *et al.* (2006). While other decay exponents have been proposed from time to time, it is natural to keep these two classical predictions in mind when examining the experimental data. However, there is a slight complication that arises when comparing these predictions with experiments: in wind-tunnel data the coefficient A can vary slowly along the test section, and this causes slight departures from the ideal values of $n = 6/5$ or $n = 10/7$, even when (4.3) or (4.4) holds true (see Krogstad & Davidson 2010). Indeed, we shall see shortly that such a slow variation of A occurs in our experiments.

Let us now estimate the decay exponents for our three grids by comparing the experimental data with the power law

$$\frac{\langle u_x^2\rangle}{U^2} = a\left[\frac{x - x_0}{\ell_0}\right]^{-n}, \tag{4.6}$$

where, as before, ℓ_0 is the integral scale at $x = 2$ m. Perhaps we should note from the outset that it is notoriously difficult to obtain reliable estimates of n. There are several reasons for this. First, as shown in Krogstad & Davidson (2010), the virtual origin x_0 in (4.6) does not correspond to the point at which the turbulence first matures, but rather is located somewhat upstream of that position, and we do not know in advance where x_0 will lie. Second, if the range of x/ℓ_0 is too short, the decay exponent becomes very sensitive to the choice of the unknown x_0. Third, if data from the inhomogeneous region close to the grid are included in the fit, then higher (and misleading) values of n are usually obtained. Fourth, for large x/ℓ_0 the turbulence intensity is low, so that noise starts to become problematic, obvious sources being electronic noise and pressure fluctuations arising from the side-wall boundary layers. In summary, then, to obtain reliable estimates of n we require that: (i) x_0 be chosen systematically and carefully, (ii) there is an extended x/ℓ_0 range, (iii) anomalous data close to the grid must be excluded and (iv) data for large x/ℓ_0 should be ignored when the noise level becomes excessive.

Figure 6 shows $\langle u_x^2\rangle/U^2$ and $\langle q^2\rangle/3U^2$, obtained using two different alignments of the x-wires, all plotted as a function of x. This log–log plot demonstrates that, for all three grids, there is a clear power-law relationship between u^2 and x. It also shows that $\langle u_x^2\rangle$ and $\langle q^2\rangle$ follow essentially the same power law. Instead of attempting a

https://doi.org/10.1017/jfm.2011.169 Published online by Cambridge University Press

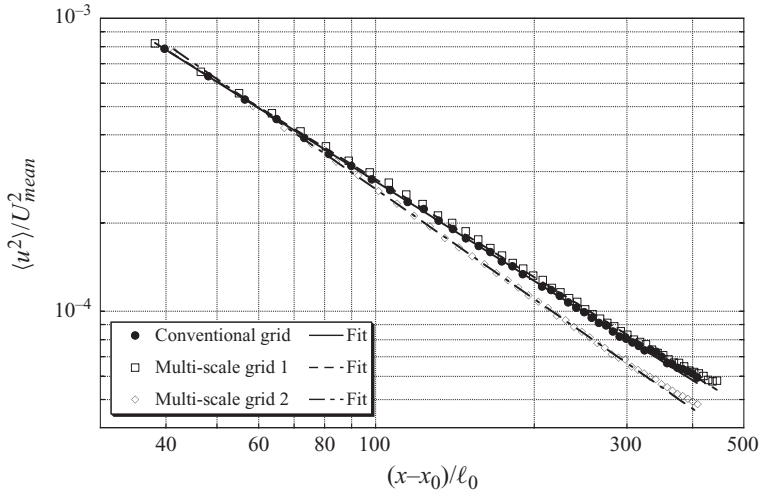


FIGURE 7. $\langle u_x^2\rangle/U^2$ versus $(x-x_0)/\ell_0$ and the corresponding best-fit power laws obtained using the regression method.

direct power-law fit to these data, it is convenient to rewrite (4.6) as

$$\ln\left[\frac{\langle u_x^2\rangle}{U^2}\right] = \ln a - n\ln\left[\frac{x-x_0}{\ell_0}\right], \tag{4.7}$$

to which a linear fit may be made. In view of the difficulty in obtaining reliable estimates of n, three different fitting procedures will be used and their results compared. All three methods are described in detail in Krogstad & Davidson (2010).

4.1. *Regression method*

Here we search for the fit that gives the smallest variance, σ^2, between the data and (4.7). The procedure works as follows. Starting with all of the data, a linear fit to (4.7) is made and σ^2 noted. Data at the most downstream location is then removed one by one until a minimum in σ^2 is obtained. This then determines x_{max}, the point beyond which noise starts to have a significant effect on the data. With x_{max} fixed, a similar procedure is then applied at the most upstream location and used to determine x_{min}, the location of the start of the admissible data. The best fit values of a, x_0 and n for these values of x_{min} and x_{max} are then taken to be the optimum values for these parameters. The exact locations of x_{min} and x_{max} vary slightly from grid to grid and between fitting to $\langle u_x^2\rangle$ and $\langle q^2\rangle$, but typically $x_{min}\approx 1.5\,\mathrm{m}$ (i.e. $\sim 60\ell_0$) and $x_{max}\approx 8\,\mathrm{m}$ (i.e. $\sim 330\ell_0$).

This procedure applied to $\langle u_x^2\rangle$ yields $n=1.13$, 1.11 and 1.25 for grids cg, $msg1$ and $msg2$ respectively, as shown in figure 7. The corresponding virtual origins are at $x_0=0.26$, 0.43 and 0.30 m. Marginally different exponents were found when applying this method to $\langle q^2\rangle$, and the range of values obtained using regression are noted in table 1, alongside the range of exponents estimated using the two procedures described in the following sections.

4.2. *Local exponent method*

Measurements of $\langle u_x^2\rangle$ were made at intervals of $\Delta x=200\,\mathrm{mm}$ or $\Delta x\approx 8.5\ell_0$ with a positioning accuracy better than $\epsilon_x=1\,\mathrm{mm}$ and so local exponents can be estimated

https://doi.org/10.1017/jfm.2011.169 Published online by Cambridge University Press

	x_0 regression method	n regression method	n local exponent method	n maximum decay range
Conventional grid	0.26 m	1.13 ± 0.02	1.14 ± 0.02	1.17 ± 0.04
Multi-scale grid 1	0.43 m	1.12 ± 0.02	1.17 ± 0.02	1.19 ± 0.03
Multi-scale grid 2	0.30 m	1.25 ± 0.02	1.25 ± 0.02	1.23 ± 0.03

TABLE 1. Estimates of the energy decay exponent n obtained using three different methods. Note that the uncertainty in n indicated above for a given method does not represent the statistical uncertainty in n, but rather the range of values obtained using a given procedure for a randomly chosen set of data.

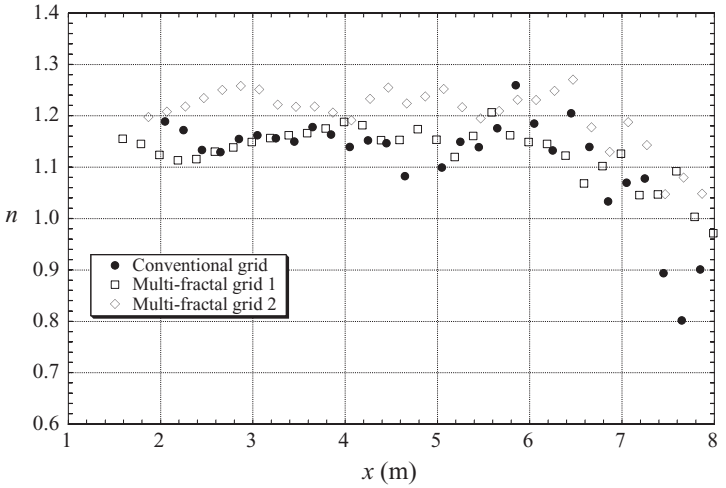


FIGURE 8. Local exponents, n, obtained for $\langle u_x^2 \rangle$ using (4.8).

using two-point differencing applied to (4.7):

$$n = -\frac{\ln\left[\dfrac{\langle u_x^2 \rangle (x + \Delta x - x_0)}{\langle u_x^2 \rangle (x - \Delta x - x_0)}\right]}{\ln\left[\dfrac{(x + \Delta x - x_0)}{(x - \Delta x - x_0)}\right]}. \tag{4.8}$$

This procedure has the advantage that the unknown coefficient a is eliminated, but the disadvantage that it is sensitive to noise. Using the values of x_0 obtained from the regression method, the estimates of n obtained using (4.8), as applied to $\langle u_x^2 \rangle$, are shown in figure 8. It is clear that these estimates of n are sensitive to noise for x greater than, say, 6.5 m. Nevertheless, reasonably constant values are found for the range $2\,\mathrm{m} < x < 6.5\,\mathrm{m}$, and averaging over this range provides a single estimate of the exponent n for each grid. Of course, this estimate varies slightly depending on whether data for $\langle u_x^2 \rangle$ or $\langle q^2 \rangle$ are analysed, and on the precise range of x used to form the average. The range of exponents thus obtained for each grid is also shown in table 1. It is reassuring that these values are close to those found by the regression method.

https://doi.org/10.1017/jfm.2011.169 Published online by Cambridge University Press

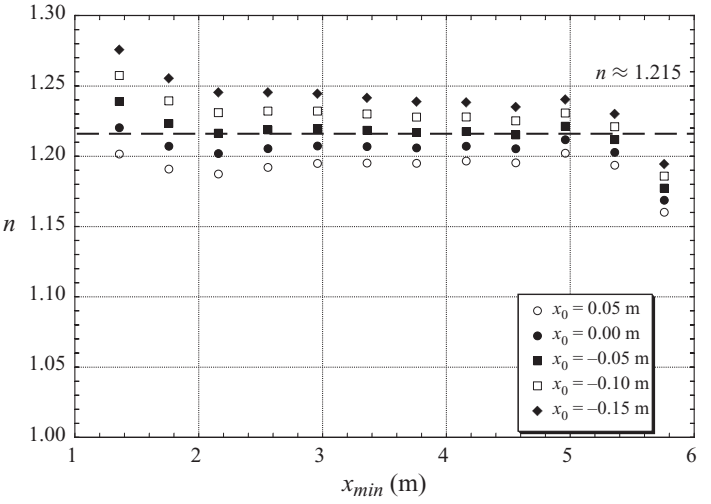


FIGURE 9. Decay exponents, n, for the grid $msg2$ as a function of x_{min} for different values of the virtual origin x_0.

4.3. *Maximum decay range method*

In this method x_0 is chosen to give the longest power-law range in x and then n is determined for that value of x_0. The procedure works as follows. First, x_{max} is fixed at the value given by the regression method (at around 8 m). Next, a series of different values of x_0 are chosen, and for each x_0 the best fit value of n is obtained for a range of values of x_{min}. The value of x_0, which gives the widest range of constant n between x_{min} and x_{max}, is then deemed to be the correct one. The exponent n then follows.

The application of this method to the conventional grid is shown in Krogstad & Davidson (2010) and demonstrated here by applying it to the $\langle q^2 \rangle$ data from $msg2$ in figure 9. As with the other methods, slightly different values of n are obtained for a given grid, depending on whether $\langle u_x^2 \rangle$ or $\langle q^2 \rangle$ are analysed. The values obtained are given in ranges indicated in table 1, where it can be seen that all three procedures generate similar exponents.

There are three striking features of table 1. First, all three grids yield decay exponents very close to the classical Saffman value of $n = 6/5$. Second, the conventional and multi-scale grids produce almost identical results (within experimental uncertainty). Third, these decay exponents are a long way from n in the range 1.7–2.0 quoted in Hurst & Vassilicos (2007) for their four fractal cross-grids. It is likely, therefore, that all three of our grids produce Saffman turbulence.

We can check the hypothesis that we have Saffman turbulence if we pre-empt our discussion of length scales in § 5. Figure 10 shows $\langle u_x^2 \rangle \ell^3 / U^2 \ell_0^3$ versus $(x - x_0)/\ell_0$ for all three grids. Recall that, in Saffman turbulence, self-similarity of the large scales requires $u^2 \ell^3 = \text{constant}$, as distinct from, say, Batchelor turbulence, in which $u^2 \ell^5 = \text{constant}$. It is clear from figure 10 that there is an initial transient, which is more or less restricted to $(x - x_0)/\ell_0 < 100$ ($x < 2.7$ m), after which $u^2 \ell^3$ is indeed more or less constant in all three cases. The scatter in this data is largely a consequence of the difficulty associated with estimating ℓ, as will be discussed in § 5.

Finally, we consider the dimensionless dissipation coefficient A in (4.5), which is normally taken to be constant during the decay of isotropic turbulence. Assuming

https://doi.org/10.1017/jfm.2011.169 Published online by Cambridge University Press

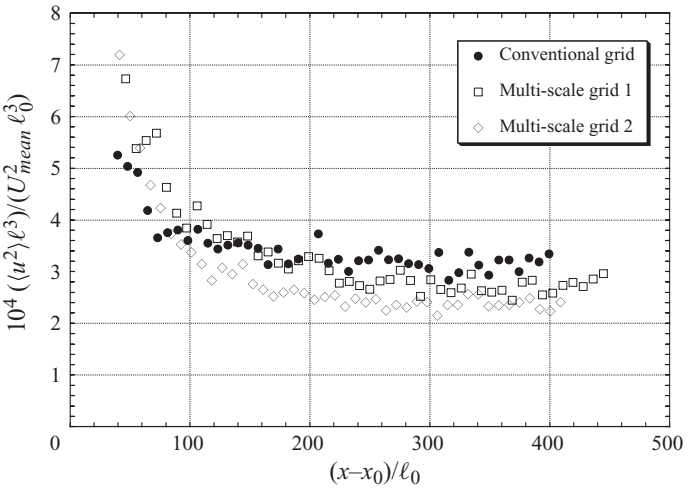


FIGURE 10. $\langle u_x^2\rangle \ell^3/U^2\ell_0^3$ versus $(x-x_0)/\ell_0$ for all three grids.

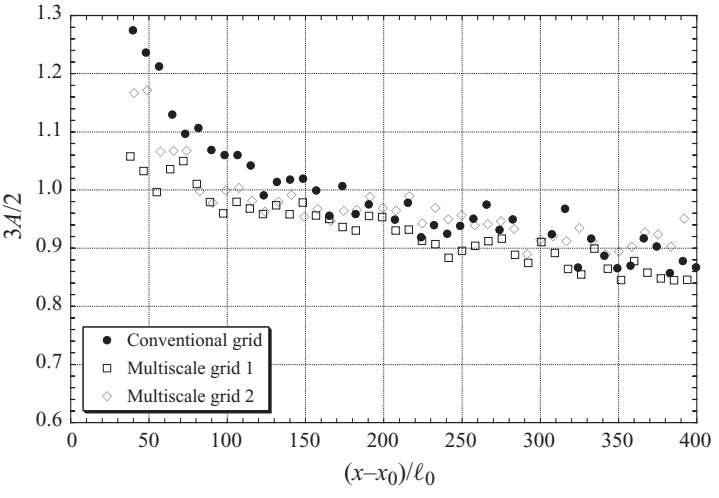


FIGURE 11. Streamwise development of A obtained from (4.9).

isotropy at the small scales, the viscous dissipation rate, ϵ, can be written as

$$\epsilon = \frac{3}{2}\frac{Au^3}{\ell} = 15\nu\left\langle\left(\frac{\partial u_x}{\partial x}\right)^2\right\rangle, \tag{4.9}$$

which allows us to estimate A from measurements of $\langle(\partial u_x/\partial x)^2\rangle$, u and ℓ. The corresponding values of A are plotted in figure 11 for all three grids as a function of $(x-x_0)/\ell_0$. Again, there is some scatter, largely due to the difficulty in estimating ℓ. Nevertheless, once the turbulence is fully developed, say for $(x-x_0)/\ell_0 > 100$, there is a slow but steady decline in A which is consistent across all three grids. As noted earlier, this slow variation in A means that, even if we have Saffman turbulence, with $u^2\ell^3 = \text{constant}$, we need not recover $n = 6/5$, as this value of n relies on A being strictly constant.

https://doi.org/10.1017/jfm.2011.169 Published online by Cambridge University Press

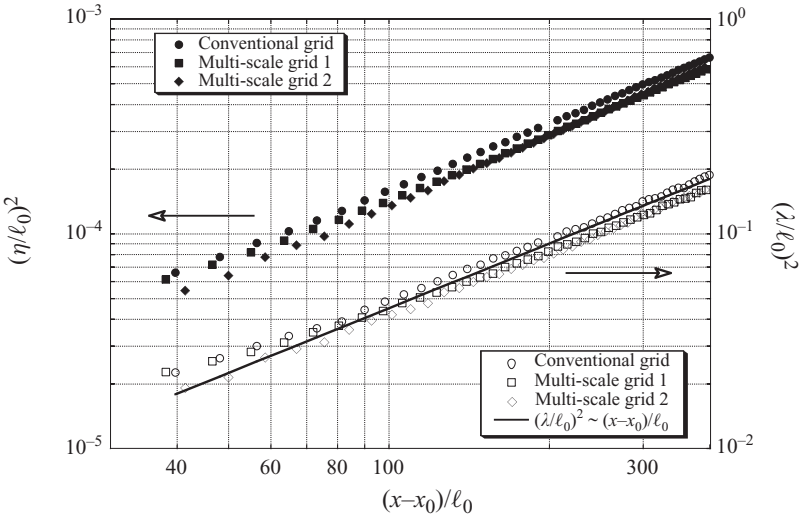


FIGURE 12. Streamwise distributions of η^2 (filled symbols) and λ^2 (open symbols). The straight line is $\lambda^2 \sim (x - x_0)$.

5. The streamwise development of length scales

We now turn to the length scales η, λ and ℓ. The Kolmogorov microscale, defined as $\eta = (\nu^3/\epsilon)^{1/4}$, can be determined from the isotropic estimate of dissipation in (4.9) or from the decay rate of $\langle q^2 \rangle$, both estimates giving virtually identical estimates for η in this type of flow, as demonstrated by Krogstad & Davidson (2010). The streamwise development of the Kolmogorov and Taylor microscales, η^2 and λ^2, is shown in figure 12.

Noting that combining (4.5) and (4.6) yields

$$\lambda^2 = \frac{10\nu\ell}{Au} = \frac{10\nu(x - x_0)}{nU}, \tag{5.1}$$

we see that λ^2 should scale as $\lambda^2 \sim (x - x_0)$, which is indeed verified in figure 12. This is, in effect, confirmation of a power-law form of energy decay.

As noted in § 2, the integral scale, ℓ, is defined in the usual way as

$$\ell = \int_0^\infty \frac{\langle u_x(x) u_x(x + r) \rangle}{\langle u_x^2 \rangle} \, \mathrm{d}r = \int_0^\infty f(r) \, \mathrm{d}r, \tag{5.2}$$

where $f(r)$ is the usual longitudinal correlation function and, in practice, $\langle u_x(x) u_x(x + r) \rangle$ is evaluated using Taylor's hypothesis. Ideally, $f(r)$ should decay monotonically to zero for large r, but in experiments $f(r)$ almost always exhibits a weak oscillatory tail which persists for many multiples of ℓ. This makes it difficult to evaluate $\int_0^\infty f(r) \, \mathrm{d}r$ accurately since it will depend on where the integral is terminated, and so the integral in (5.2) was only taken up to the first zero crossing, which introduces a small systematic error. As a result, there is some uncertainty in the calculated values of ℓ. Our estimates of ℓ for all three grids are shown in figure 13.

Evidently, ℓ exhibits considerably more scatter than η or λ, but it is clear that the development of ℓ is similar for all three grids and follows a power law. Moreover, power-law energy decay with constant A demands $\ell \sim ut$, and so Saffman turbulence predicts $\ell \sim (x - x_0)^{0.4}$, provided we ignore the slow decline in A. This is shown

https://doi.org/10.1017/jfm.2011.169 Published online by Cambridge University Press

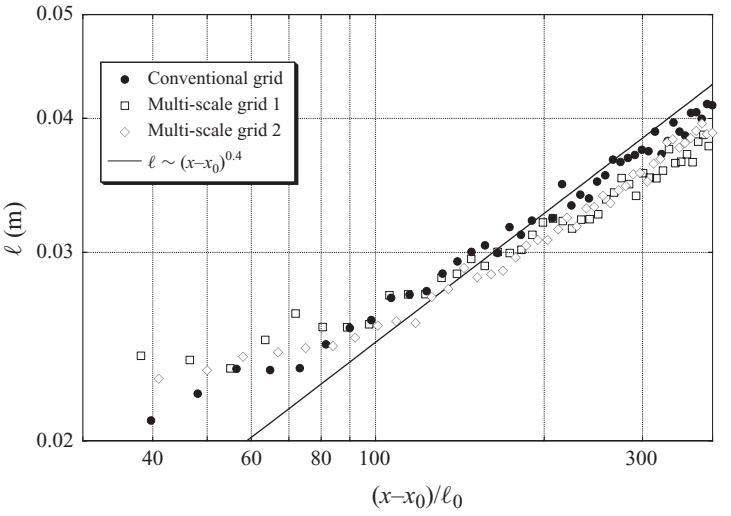


FIGURE 13. The integral scale, ℓ, as a function of $(x - x_0)/\ell_0$. The solid line is $\ell \sim (x - x_0)^{0.4}$.

in figure 13 for comparison and the data for all cases follow such a trend for $(x - x_0)/\ell > 100$.

6. Spectral development of the turbulence

We have seen that, as far as the behaviour of the integral scales u and ℓ is concerned, the conventional and multi-scale grids behave in almost identical ways. However, it might be argued that, because energy is injected across the scales with a multi-scale grid, the evolution of the energy spectrum may exhibit non-classical features. So we conclude by comparing the spectra of the multi-scale and conventional grids. We shall focus on the usual one-dimensional spectrum, $F_{11}(k)$, defined by the transform pair

$$F_{11}(k) = \frac{2}{\pi}\int_0^\infty \langle u_x(x)u_x(x+r)\rangle \cos(kr)\,\mathrm{d}r, \tag{6.1}$$

$$\langle u_x(x)u_x(x+r)\rangle = \int_0^\infty F_{11}(k)\cos(kr)\,\mathrm{d}k. \tag{6.2}$$

We first consider the issue of the energy injection scales for the multi-scale grids. Figure 14 shows $F_{11}(k)$ for these two grids, measured just downstream of the mesh (at $x \approx 1.3\,\mathrm{m}$) and normalized by the Kolmogorov microscales η and υ. The mesh sizes M_i and bar widths t_i are marked on the horizontal axis using the rule of thumb that $k = \pi/\ell$. It is clear that in both cases the range of geometric scales spans most of the turbulent spectrum.

Next, there is the issue of whether or not the turbulence produced by the multi-scale grids behaves in the classical way, with the spectrum collapsing at high k when normalized by the microscales η and υ, and at low k when normalized by the integral scales ℓ and u. Figure 15 shows $F_{11}(k)$ for grid $msg1$ measured at four different streamwise locations and normalized by η and υ (figure 15a) and ℓ and u (figure 15b). In the case of figure 15(a), there is excellent collapse of the spectra at high k and no collapse at low k, while in figure 15(b) there is reasonable collapse at low k and no collapse at high k. The same plots are given for $msg2$ in figure 16 and

https://doi.org/10.1017/jfm.2011.169 Published online by Cambridge University Press

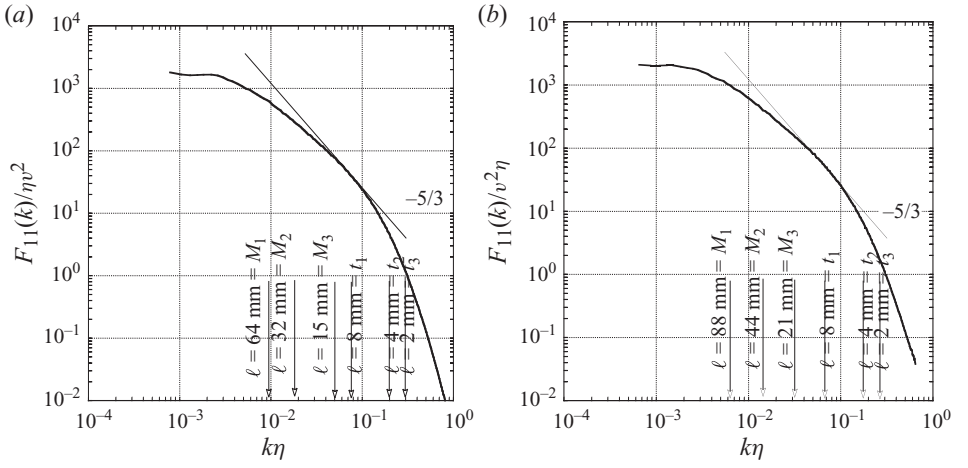


FIGURE 14. $F_{11}(k)$, normalized by the Kolmogorov microscales η and v, for (*a*) *msg*1 and (*b*) *msg*2, measured near the grid at $x \approx 1.3$ m.

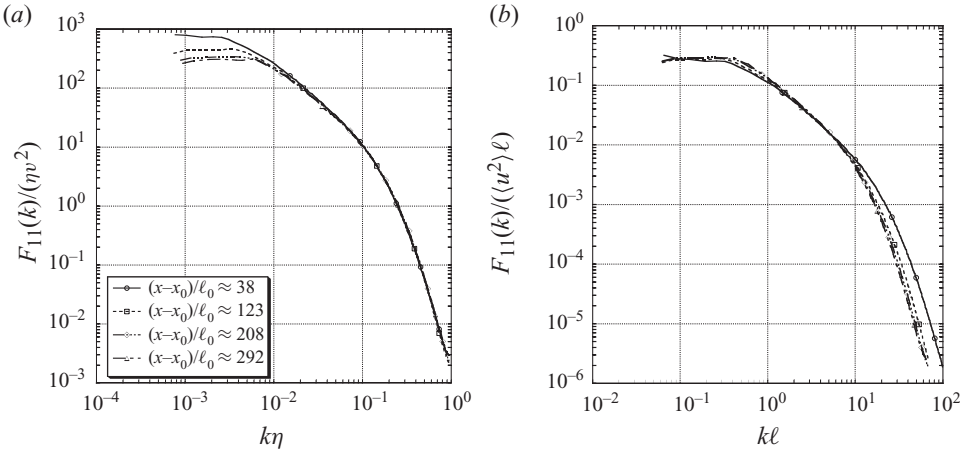


FIGURE 15. $F_{11}(k)$ for grid *msg*1 measured at four streamwise locations and normalized by (*a*) η and v and (*b*) ℓ and u.

again there is excellent collapse at high k when normalized by η and v, and at low k when scaled by ℓ and u also in this case. Once again, we see that the turbulence produced by the multi-scale grids behaves in a classical manner.

Finally, we compare spectra at the same location generated by the three different grids. Figure 17 shows $F_{11}(k)$ for all three grids, normalized by the integral scales ℓ and u, at $\ell \sim (x - x_0)/\ell_0 \approx 40$ (figure 17*a*) and $\ell \sim (x - x_0)/\ell_0 \approx 290$ (figure 17*b*). There is excellent collapse at both streamwise locations, confirming that the nature of the turbulence coming off the conventional and multi-scale grids is essentially the same. The same information may be examined in real space using the longitudinal structure function

$$\langle (\Delta u_x)^2 \rangle = \langle (u_x(x + r) - u_x(x))^2 \rangle = 2 \langle u_x^2 \rangle - 2 \langle u_x(x) u_x(x + r) \rangle, \tag{6.3}$$

which, crudely speaking, acts as a cumulative index of all energy held in structures smaller than scale r. Figure 18 shows $\langle (\Delta u_x)^2 \rangle / 2 \langle u_x^2 \rangle$ plotted against r/ℓ at the same

https://doi.org/10.1017/jfm.2011.169 Published online by Cambridge University Press

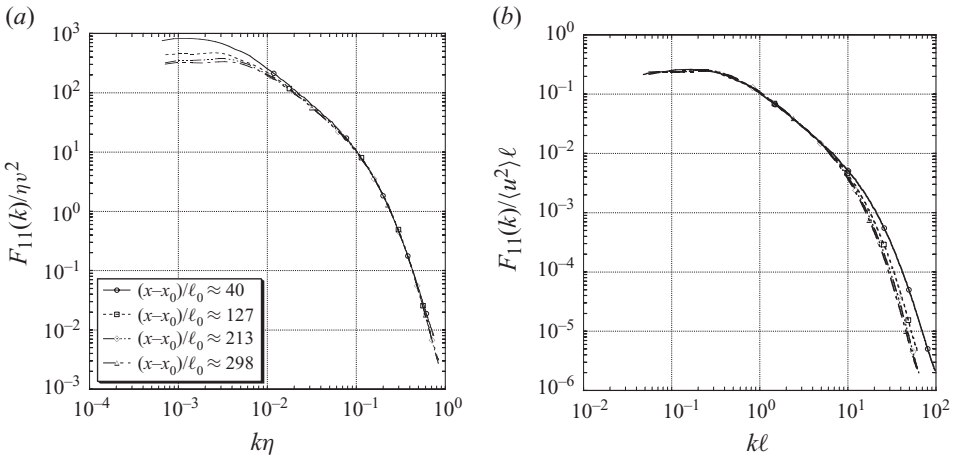


FIGURE 16. $F_{11}(k)$ for grid $msg2$ measured at four streamwise locations and normalized by (*a*) η and υ and (*b*) ℓ and u.

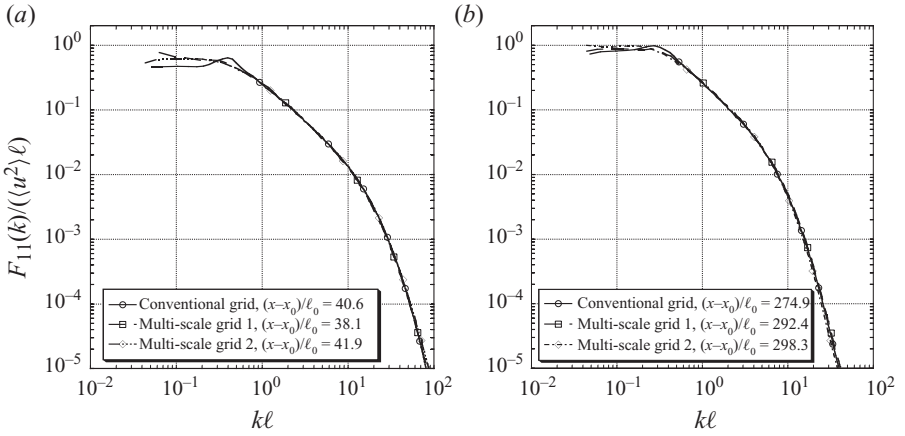


FIGURE 17. $F_{11}(k)$ for all three grids, normalized by the integral scales ℓ and u at (*a*) $(x - x_0)/\ell_0 \approx 40$ and (*b*) $(x - x_0)/\ell_0 \approx 290$.

two streamwise locations as figure 17. Again, it can be seen that there is good collapse at both locations.

7. Conclusions

Our primary findings are twofold. First, it seems that Saffman's decay law is reasonably robust, since the energy decay exponents for all three grids are close to Saffman's classical prediction of $n = 6/5$. Second, the multi-scale grids used here produce almost identical results to the equivalent classical grid. In particular, all three flows exhibit remarkably similar streamwise distributions of Re_λ (figure 2), flatness and skewness (figure 5), and dimensionless decay coefficient A (figure 11). It is also worth noting that the spectra for the multi-scale grids exhibit classical Kolmogorov scaling, with $E(k)$ collapsing on ℓ and u at low k, and on η and υ at high k.

Our findings contradict those of some previous studies which report unusual behaviour behind similar multi-scale grids, in particular, a very high-energy decay

https://doi.org/10.1017/jfm.2011.169 Published online by Cambridge University Press

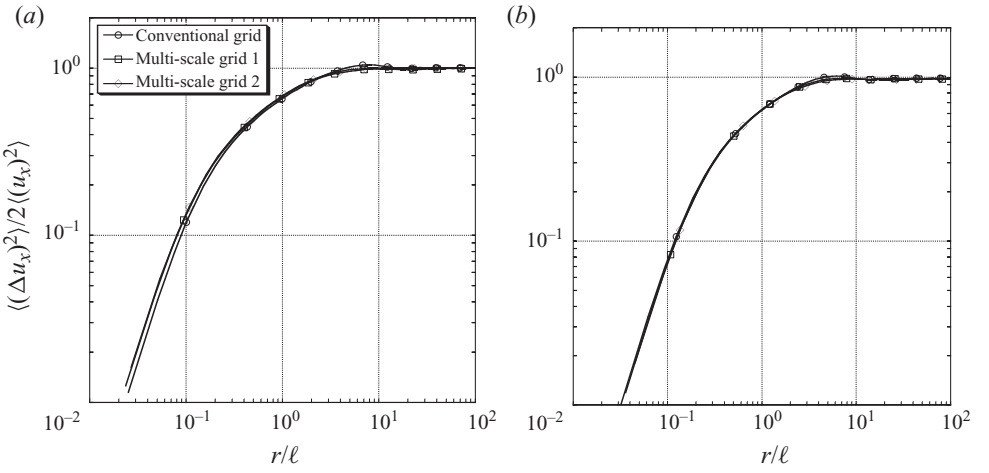


FIGURE 18. $\langle(\Delta u_x)^2\rangle/2\langle u_x^2\rangle$ plotted against r/ℓ for all three grids at (*a*) $(x-x_0)/\ell_0 \approx 40$ and (*b*) $(x-x_0)/\ell_0 \approx 290$.

exponent of around $n \sim 2.0$ and unusually high values of Re_λ. A decay exponent of $n \sim 2.0$ is particularly worrying as the theoretical maximum for n (assuming the dimensionless decay coefficient, A, is constant) is $n = 10/7$. However, these earlier measurements were taken much closer to the grid where the flow exhibits initial grid-dependent inhomogeneities; inhomogeneities which, according to the present data, disappear further downstream.

Appendix. Classical decay exponents

The classical decay exponents of isotropic turbulence, including those of Kolmogorov (1941) and Saffman (1967), are obtained as follows (see Ossai & Lesieur 2000; Davidson 2004, 2009; Ishida *et al.* 2006 for more details). We start with the result that, in fully developed turbulence, $E(k \to 0) = c_m k^m$, where $c_m \sim u^2 \ell^{m+1}$ and $c_m = \text{constant}$ for $m \leqslant 4$. Self-similarity of the large scales then demands $u^2 \ell^{m+1} = \text{constant}$ for $m \leqslant 4$. When combined with the zeroth law (4.5), this yields

$$\frac{u^2}{u_0^2} = \left[1 + \frac{A}{n}\frac{u_0 t}{\ell_0}\right]^{-n}, \qquad n = 2 - \frac{4}{m+3}, \tag{A 1}$$

where the subscripts 0 indicate values at $t = 0$. The smallest value of m is 2, since lower values require that the spectral tensor diverges as $k \to 0$. On the other hand, the largest value is $m = 4$, as higher values spontaneously convert to $m = 4$ during an initial transient. Thus, the classical range of decay exponents is $6/5 \leqslant n \leqslant 10/7$.

REFERENCES

COMTE-BELLOT, G. & CORRSIN, S. 1966 The use of a contraction to improve the isotropy of grid-generated turbulence. *J. Fluid Mech.* **25**, 657–682.

DAVIDSON, P. A. 2004 *Turbulence: An Introduction for Scientists and Engineers.* Oxford University Press.

DAVIDSON, P. A. 2009 The role of angular momentum conservation in homogenous turbulence. *J. Fluid Mech.* **632**, 329–358.

https://doi.org/10.1017/jfm.2011.169 Published online by Cambridge University Press

Gad-el-Hak, M. & Corrsin, S. 1974 Measurements of the nearly isotropy turbulence behind a uniform jet grid. *J. Fluid Mech.* **62**, 115–143.

George, W. K. & Wang, H. 2009 The exponential decay of homogeneous turbulence. *Phys. Fluids* **21** (2), 025108.

Hosokawa, I. 2008 One-point velocity statistics in decaying homogeneous isotropic turbulence. *Phys. Rev.* E **78**, 066312.

Hurst, D. & Vassilicos, J. C. 2007 Scalings and decay of fractal-generated turbulence. *Phys. Fluids* **19** (3), 035103.

Ishida, T., Davidson, P. A. & Kaneda Y. 2006 On the decay of isotropic turbulence. *J. Fluid Mech.* **564**, 455–475.

Kolmogorov, A. N. 1941 On the degeneration of isotropic turbulence in an incompressible viscous fluid. *Dokl. Akad. Nauk. SSSR* **31** (6), 538–541.

Krogstad, P.-Å. & Davidson, P. A. 2010 Is grid turbulence Saffman turbulence? *J. Fluid Mech.* **642**, 373–394.

Nagata, K., Suzuki, H., Sakai, Y., Hayase, T. & Kubo, T. 2008 Direct numerical simulation of turbulence characteristics generated by fractal grids. *Intl Rev. Phys.* **2** (6), 400–409.

Ossai, S. & Lesieur, M. M. 2000 Energy backscatter in large-scale simulations of three dimensional incompressible isotropic turbulence. *J. Turbulence* **1**, 010.

Saffman, P. J. 1967 The large-scale structure of homogeneous turbulence. *J. Fluid Mech.* **27**, 581–593.

https://doi.org/10.1017/jfm.2011.169 Published online by Cambridge University Press